Time-shift imaging condition in seismic migration[a]

Paul Sava and Sergey Fomel[1]

ABSTRACT

Seismic imaging based on single-scattering approximation is based on analysis of the match between the source and receiver wavefields at every image location. Wavefields at depth are functions of space and time and are reconstructed from surface data either by integral methods (Kirchhoff migration) or by differential methods (reverse-time or wavefield extrapolation migration). Different methods can be used to analyze wavefield matching, of which cross-correlation is a popular option. Implementation of a simple imaging condition requires time cross-correlation of source and receiver wavefields, followed by extraction of the zero time lag. A generalized imaging condition operates by cross-correlation in both space and time, followed by image extraction at zero time lag. Images at different spatial cross-correlation lags are indicators of imaging accuracy and are also used for image angle-decomposition.

In this paper, we introduce an alternative prestack imaging condition in which we preserve multiple lags of the time cross-correlation. Prestack images are described as functions of time-shifts as opposed to space-shifts between source and receiver wavefields. This imaging condition is applicable to migration by Kirchhoff, wavefield extrapolation or reverse-time techniques. The transformation allows construction of common-image gathers presented as function of either time-shift or reflection angle at every location in space. Inaccurate migration velocity is revealed by angle-domain common-image gathers with non-flat events. Computational experiments using a synthetic dataset from a complex salt model demonstrate the main features of the method.

INTRODUCTION

A key challenge for imaging in complex areas is accurate determination of a velocity model in the area under investigation. Migration velocity analysis is based on the principle that image accuracy indicators are optimized when data are correctly imaged. A common procedure for velocity analysis is to examine the alignment of images created with multi-offset data. An optimal choice of image analysis can be done in the angle domain which is free of some complicated artifacts present in surface offset gathers in complex areas (Stolk and Symes, 2004).

[1]**e-mail:** psava@mines.edu, sergey.fomel@beg.utexas.edu

Migration velocity analysis after migration by wavefield extrapolation requires image decomposition in scattering angles relative to reflector normals. Several methods have been proposed for such decompositions (de Bruin et al., 1990; Prucha et al., 1999; Mosher and Foster, 2000; Rickett and Sava, 2002; Xie and Wu, 2002; Sava and Fomel, 2003; Soubaras, 2003; Fomel, 2004; Biondi and Symes, 2004). These procedures require decomposition of extrapolated wavefields in variables that are related to the reflection angle.

A key component of such image decompositions is the imaging condition. A careful implementation of the imaging condition preserves all information necessary to decompose images in their angle-dependent components. The challenge is efficient and reliable construction of these angle-dependent images for velocity or amplitude analysis.

In migration with wavefield extrapolation, a prestack imaging condition based on spatial shifts of the source and receiver wavefields allows for angle-decomposition (Rickett and Sava, 2002; Sava and Fomel, 2005). Such formed angle-gathers describe reflectivity as a function of reflection angles and are powerful tools for migration velocity analysis (MVA) or amplitude versus angle analysis (AVA). However, due to the large expense of space-time cross-correlations, especially in three dimensions, this imaging methodology is not used routinely in data processing.

This paper presents a different form of imaging condition. The key idea of this new method is to use time-shifts instead of space-shifts between wavefields computed from sources and receivers. Similarly to the space-shift imaging condition, an image is built by space-time cross-correlations of subsurface wavefields, and multiple lags of the time cross-correlation are preserved in the image. Time-shifts have physical meaning that can be related directly to reflection geometry, similarly to the procedure used for space-shifts. Furthermore, time-shift imaging is cheaper to apply than space-shift imaging, and thus it might alleviate some of the difficulties posed by costly cross-correlations in 3D space-shift imaging condition.

The idea of a time-shift imaging condition is related to the idea of depth focusing analysis (Faye and Jeannot, 1986; MacKay and Abma, 1992, 1993; Nemeth, 1995, 1996). The main novelty of our approach is that we employ time-shifting to construct angle-domain gathers for prestack depth imaging.

The time-shift imaging concept is applicable to Kirchhoff migration, migration by wavefield extrapolation, or reverse-time migration. We present a theoretical analysis of this new imaging condition, followed by a physical interpretation leading to angle-decomposition. Finally, we illustrate the method with images of the complex Sigsbee 2A dataset (Paffenholz et al., 2002).

IMAGING CONDITION IN WAVE-EQUATION IMAGING

A traditional imaging condition for shot-record migration, often referred-to as UD^* imaging condition (Claerbout, 1985), consists of time cross-correlation at every image location between the source and receiver wavefields, followed by image extraction at zero time:

$$U\left(\mathbf{m}, t\right) = U_r\left(\mathbf{m}, t\right) * U_s\left(\mathbf{m}, t\right) , \tag{1}$$

$$R\left(\mathbf{m}\right) = U\left(\mathbf{m}, t = 0\right) , \tag{2}$$

where the symbol $*$ denotes cross-correlation in time. Here, $\mathbf{m} = [m_x, m_y, m_z]$ is a vector describing the locations of image points, $U_s(\mathbf{m}, t)$ and $U_r(\mathbf{m}, t)$ are source and receiver wavefields respectively, and $R(\mathbf{m})$ denotes a migrated image. A final image is obtained by summation over shots.

Space-shift imaging condition

A generalized prestack imaging condition (Sava and Fomel, 2005) estimates image reflectivity using cross-correlation in space and time, followed by image extraction at zero time:

$$U\left(\mathbf{m}, \mathbf{h}, t\right) = U_r\left(\mathbf{m} + \mathbf{h}, t\right) * U_s\left(\mathbf{m} - \mathbf{h}, t\right) , \tag{3}$$

$$R\left(\mathbf{m}, \mathbf{h}\right) = U\left(\mathbf{m}, \mathbf{h}, t = 0\right) . \tag{4}$$

Here, $\mathbf{h} = [h_x, h_y, h_z]$ is a vector describing the space-shift between the source and receiver wavefields prior to imaging. Special cases of this imaging condition are horizontal space-shift (Rickett and Sava, 2002) and vertical space-shift (Biondi and Symes, 2004).

For computational reasons, this imaging condition is usually implemented in the Fourier domain using the expression

$$R\left(\mathbf{m}, \mathbf{h}\right) = \sum_\omega U_r\left(\mathbf{m} + \mathbf{h}, \omega\right) U_s^*\left(\mathbf{m} - \mathbf{h}, \omega\right) . \tag{5}$$

The $*$ sign represents a complex conjugate applied on the receiver wavefield U_s in the Fourier domain.

Time-shift imaging condition

Another possible imaging condition, advocated in this paper, involves shifting of the source and receiver wavefields in time, as opposed to space, followed by image extraction at zero time:

$$U\left(\mathbf{m}, t, \tau\right) = U_r\left(\mathbf{m}, t + \tau\right) * U_s\left(\mathbf{m}, t - \tau\right) , \tag{6}$$

$$R\left(\mathbf{m}, \tau\right) = U\left(\mathbf{m}, \tau, t = 0\right) . \tag{7}$$

Here, τ is a scalar describing the time-shift between the source and receiver wavefields prior to imaging. This imaging condition can be implemented in the Fourier domain using the expression

$$R(\mathbf{m}, \tau) = \sum_{\omega} U_r(\mathbf{m}, \omega) U_s^*(\mathbf{m}, \omega) e^{2i\omega\tau} , \qquad (8)$$

which simply involves a phase-shift applied to the wavefields prior to summation over frequency ω for imaging at zero time.

Space-shift and time-shift imaging condition

To be even more general, we can formulate an imaging condition involving both space-shift and time-shift, followed by image extraction at zero time:

$$U(\mathbf{m}, \mathbf{h}, t) = U_r(\mathbf{m} + \mathbf{h}, t + \tau) * U_s(\mathbf{m} - \mathbf{h}, t - \tau) , \qquad (9)$$
$$R(\mathbf{m}, \mathbf{h}, \tau) = U(\mathbf{m}, \mathbf{h}, \tau, t = 0) . \qquad (10)$$

However, the cost involved in this transformation is large, so this general form does not have immediate practical value. Imaging conditions described by equations (3)-(4) and (6)-(7) are special cases of equations (9)-(10) for $\mathbf{h} = 0$ and $\tau = 0$, respectively.

ANGLE TRANSFORMATION IN WAVE-EQUATION IMAGING

Using the definitions introduced in the preceding section, we can make the standard notations for source and receiver coordinates: $\mathbf{s} = \mathbf{m} - \mathbf{h}$ and $\mathbf{r} = \mathbf{m} + \mathbf{h}$. The traveltime from a source to a receiver is a function of all spatial coordinates of the seismic experiment $t = t(\mathbf{m}, \mathbf{h})$. Differentiating t with respect to all components of the vectors $\mathbf{m}$ and $\mathbf{h}$, and using the standard notations $\mathbf{p}_\alpha = \nabla_\alpha t$, where $\alpha = \{\mathbf{m}, \mathbf{h}, \mathbf{s}, \mathbf{r}\}$, we can write:

$$\mathbf{p_m} = \mathbf{p_r} + \mathbf{p_s} , \qquad (11)$$
$$\mathbf{p_h} = \mathbf{p_r} - \mathbf{p_s} . \qquad (12)$$

From equations (11)-(12), we can write

$$2\mathbf{p_s} = \mathbf{p_m} - \mathbf{p_h} , \qquad (13)$$
$$2\mathbf{p_r} = \mathbf{p_m} + \mathbf{p_h} . \qquad (14)$$

By analyzing the geometric relations of various vectors at an image point (Figure 1), we can write the following trigonometric expressions:

$$|\mathbf{p_h}|^2 = |\mathbf{p_s}|^2 + |\mathbf{p_r}|^2 - 2|\mathbf{p_s}||\mathbf{p_r}|\cos(2\theta) , \qquad (15)$$
$$|\mathbf{p_m}|^2 = |\mathbf{p_s}|^2 + |\mathbf{p_r}|^2 + 2|\mathbf{p_s}||\mathbf{p_r}|\cos(2\theta) . \qquad (16)$$
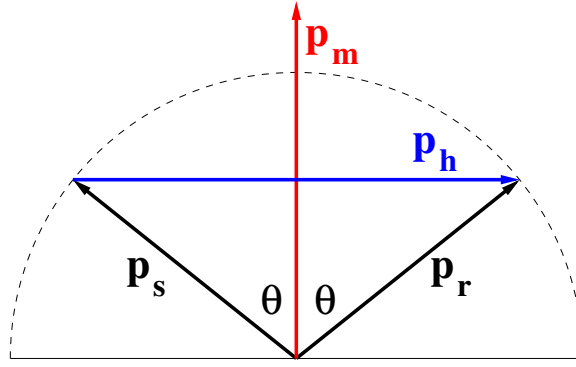
Figure 1: Geometric relations between ray vectors at a reflection point.

Equations (15)-(16) relate wavefield quantities, $\mathbf{p_h}$ and $\mathbf{p_m}$, to a geometric quantity, reflection angle θ. Analysis of these expressions provide sufficient information for complete decompositions of migrated images in components for different reflection angles.

Space-shift imaging condition

Defining $\mathbf{k_m}$ and $\mathbf{k_h}$ as location and offset wavenumber vectors, and assuming $|\mathbf{p_s}| = |\mathbf{p_r}| = s$, where $s\,(\mathbf{m})$ is the slowness at image locations, we can replace $|\mathbf{p_m}| = |\mathbf{k_m}|/\omega$ and $|\mathbf{p_h}| = |\mathbf{k_h}|/\omega$ in equations (15)-(16):

$$|\mathbf{k_h}|^2 = 2(\omega\,s)^2(1 - \cos 2\theta) , \tag{17}$$
$$|\mathbf{k_m}|^2 = 2(\omega\,s)^2(1 + \cos 2\theta) . \tag{18}$$

Using the trigonometric identity

$$\cos(2\theta) = \frac{1 - \tan^2\theta}{1 + \tan^2\theta} , \tag{19}$$

we can eliminate from equations (17)-(18) the dependence on frequency and slowness, and obtain an angle decomposition formulation after imaging by expressing $\tan\theta$ as a function of position and offset wavenumbers $(\mathbf{k_m}, \mathbf{k_h})$:

$$\tan\theta = \frac{|\mathbf{k_h}|}{|\mathbf{k_m}|} . \tag{20}$$

We can construct angle-domain common-image gathers by transforming prestack migrated images using equation (20)

$$R\,(\mathbf{m}, \mathbf{h}) \Longrightarrow R\,(\mathbf{m}, \theta) . \tag{21}$$

In 2D, this transformation is equivalent with a slant-stack on migrated offset gathers. For 3D, this transformation is described in more detail by Fomel (2004) or Sava and Fomel (2005).

Time-shift imaging condition

Using the same definitions as the ones introduced in the preceding subsection, we can re-write equation (18) as

$$|\mathbf{p_m}|^2 = 4s^2 \cos^2 \theta \; , \tag{22}$$

from which we can derive an expression for angle-transformation after time-shift prestack imaging:

$$\cos \theta = \frac{|\mathbf{p_m}|}{2s} \; . \tag{23}$$

Relation (23) can be interpreted using ray parameter vectors at image locations (Figure 2). Angle-domain common-image gathers can be obtained by transforming
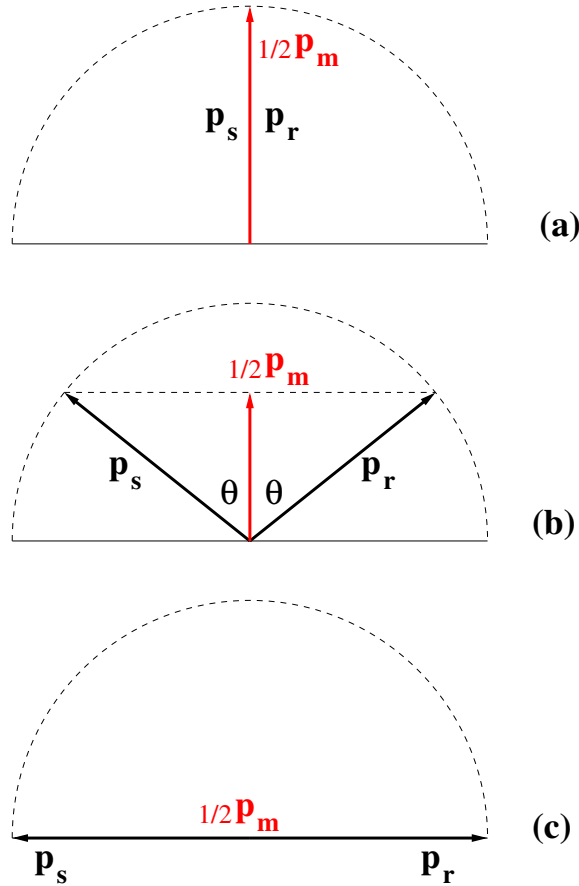
Figure 2: Interpretation of angle-decomposition based on equation (23) for time-shift gathers.

prestack migrated images using equation (23):

$$R(\mathbf{m}, \tau) \Longrightarrow R(\mathbf{m}, \theta) \; . \tag{24}$$

Equation (23) can be written as

$$\cos^2 \theta = \frac{|\nabla_{\mathbf{m}} 2\tau|^2}{4s^2(\mathbf{m})} = \frac{\tau_x^2 + \tau_y^2 + \tau_z^2}{s^2(x, y, z)} \; , \tag{25}$$

where τ_x, τ_y, τ_z are partial derivatives of τ relative to x, y, z. We can rewrite equation (25) as

$$\cos^2 \theta = \frac{\tau_z^2}{s^2 (x, y, z)} \left(1 + z_x^2 + z_y^2\right) \ , \tag{26}$$

where z_x, z_y denote partial derivative of coordinate z relative to coordinates x and y, respectively. Equation (26) describes an algorithm in two steps for angle-decomposition after time-shift imaging: compute $\cos \theta$ through a slant-stack in $z - \tau$ panels (find a change in τ with respect to z), then apply a correction using the migration slowness s and a function of the structural dips $\sqrt{1 + z_x^2 + z_y^2}$.

MOVEOUT ANALYSIS
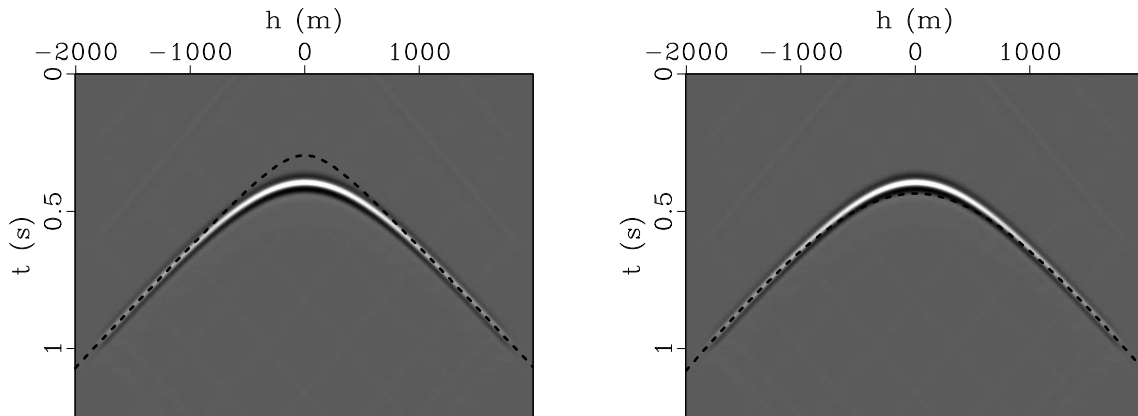
Figure 3: An image is formed when the Kirchoff stacking curve (dashed line) touches the true reflection response. Left: the case of under-migration; right: over-migration.

We can use the Kirchhoff formulation to analyze the moveout behavior of the time-shift imaging condition in the simplest case of a flat reflector in a constant-velocity medium (Figures 3-5).

The synthetic data are imaged using shot-record wavefield extrapolation migration. Figure 4 shows offset common-image gathers for three different migration slownesses s, one of which is equal to the modeling slowness s_0. The left column corresponds to the space-shift imaging condition and the right column corresponds to the time-shift imaging condition.

For the space-shift CIGs imaged with correct slowness, left column in Figure 4, the energy is focused at zero offset, but it spreads in a region of offsets when the slowness is wrong. Slant-stacking produces the images in left column of Figure 5.

For the time-shift CIGs imaged with correct slowness, right column in Figure 4, the energy is distributed along a line with a slope equal to the local velocity at the reflector position, but it spreads around this region when the slowness is wrong. Slant-stacking produces the images in the right column of Figure 5.
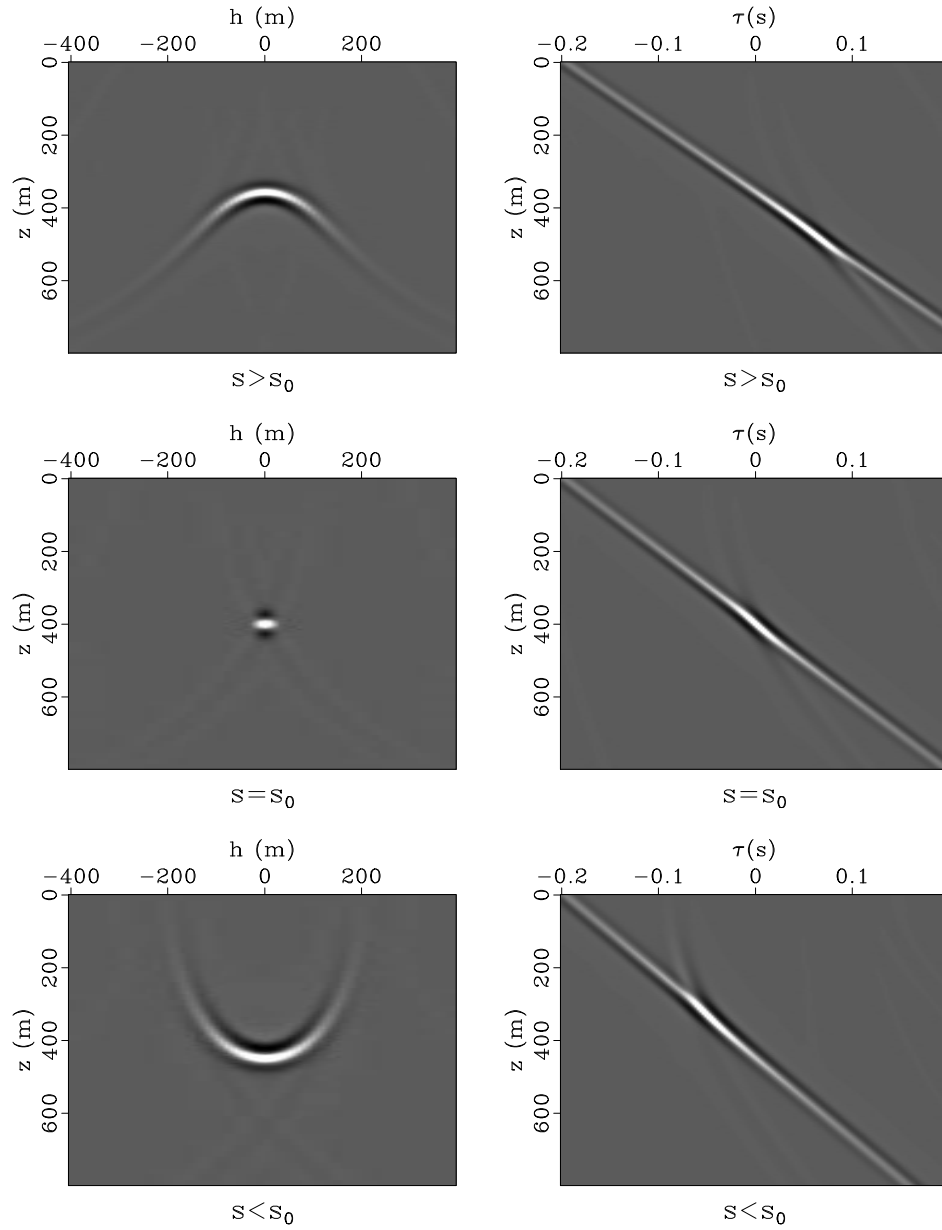
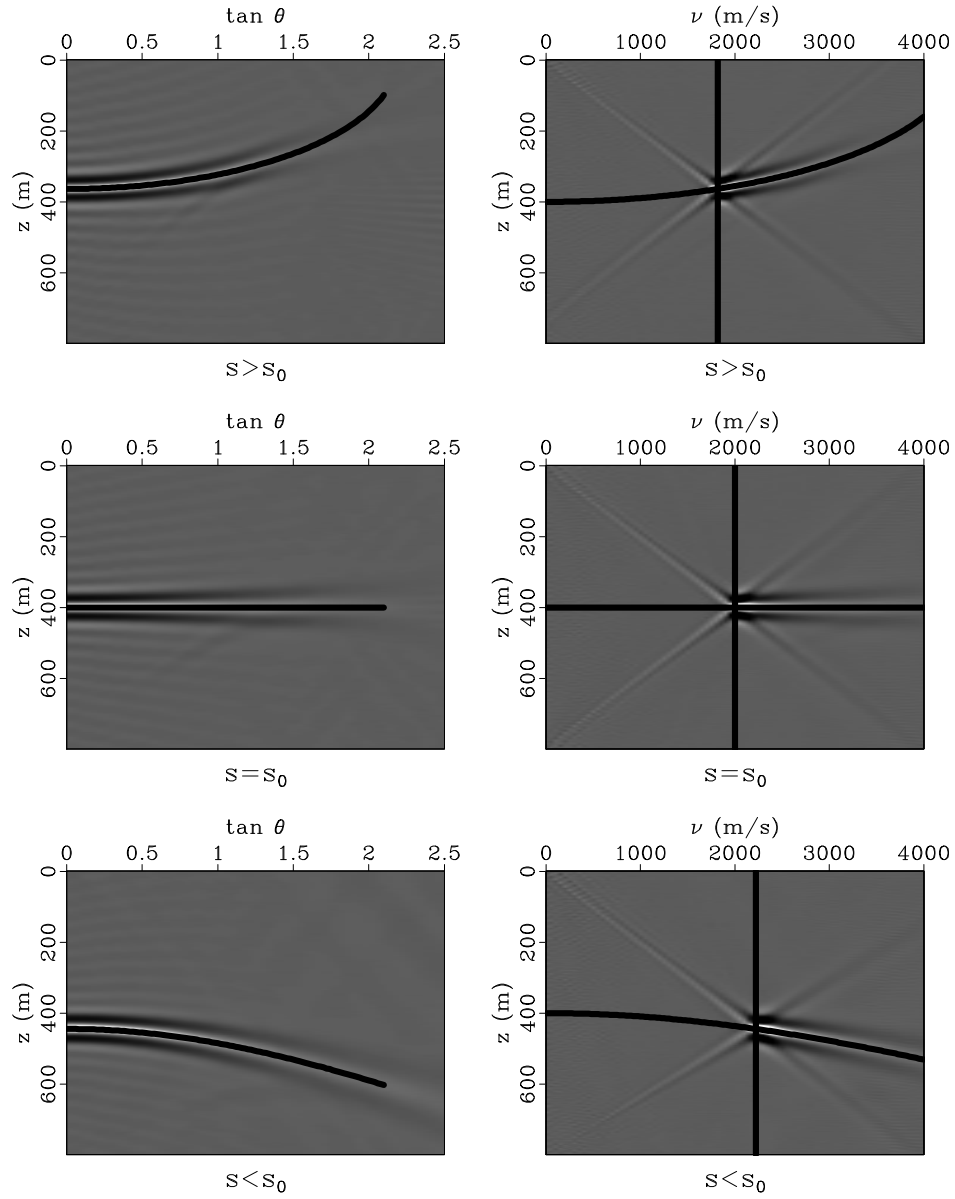Figure 4: Common-image gathers for space-shift imaging (left column) and time-shift imaging (right column).

Figure 5: Common-image gathers after slant-stack for space-shift imaging (left column) and for time-shift imaging (right column). The vertical line indicates the migration velocity.

Let s_0 and z_0 represent the true slowness and reflector depth, and s and z stand for the corresponding quantities used in migration. An image is formed when the Kirchoff stacking curve $t(\hat{h}) = 2\,s\,\sqrt{z^2 + \hat{h}^2} + 2\,\tau$ touches the true reflection response $t_0(\hat{h}) = 2\,s_0\,\sqrt{z_0^2 + \hat{h}^2}$ (Figure 3). Solving for $\hat{h}$ from the envelope condition $t'(\hat{h}) = t_0'(\hat{h})$ yields two solutions:

$$\hat{h} = 0 \tag{27}$$

and

$$\hat{h} = \sqrt{\frac{s_0^2 z^2 - s^2 z_0^2}{s^2 - s_0^2}} \; . \tag{28}$$

Substituting solutions 27 and 28 in the condition $t(\hat{h}) = t_0(\hat{h})$ produces two images in the $\{z, \tau\}$ space. The first image is a straight line

$$z(\tau) = \frac{z_0\,s_0 - \tau}{s} \; , \tag{29}$$

and the second image is a segment of the second-order curve

$$z(\tau) = \sqrt{z_0^2 + \frac{\tau^2}{s^2 - s_0^2}} \; . \tag{30}$$

Applying a slant-stack transformation with $z = z_1 - \nu\,\tau$ turns line (29) into a point $\{z_0\,s_0/s, 1/s\}$ in the $\{z_1, \nu\}$ space, while curve (30) turns into the curve

$$z_1(\nu) = z_0\,\sqrt{1 + \nu^2\,(s_0^2 - s^2)} \; . \tag{31}$$

The curvature of the $z_1(\nu)$ curve at $\nu = 0$ is a clear indicator of the migration velocity errors.

By contrast, the moveout shape $z(h)$ appearing in wave-equation migration with the lateral-shift imaging condition is (Bartana et al., 2005)

$$z(h) = s_0\,\sqrt{\frac{z_0^2}{s^2} + \frac{h^2}{s^2 - s_0^2}} \; . \tag{32}$$

After the slant transformation $z = z_1 + h\,\tan\theta$, the moveout curve (32) turns into the curve

$$z_1(\theta) = \frac{z_0}{s}\,\sqrt{s_0^2 + \tan^2\theta\,(s_0^2 - s^2)} \; , \tag{33}$$

which is applicable for velocity analysis. A formal connection between ν-parameterization in equation (31) and θ-parameterization in equation (33) is given by

$$\tan^2\theta = s^2\,\nu^2 - 1 \; , \tag{34}$$

or

$$\cos\theta = \frac{1}{\nu s} = \frac{\tau_z}{s} \; , \tag{35}$$

where $\tau_z = \frac{\partial\tau}{\partial z}$. Equation (35) is a special case of equation (23) for flat reflectors. Curves of shape (31) and (33) are plotted on top of the experimental moveouts in Figure 5.

TIME-SHIFT IMAGING IN KIRCHHOFF MIGRATION

The imaging condition described in the preceding section has an equivalent formulation in Kirchhoff imaging. Traditional construction of common-image gathers using Kirchhoff migration is represented by the expression

$$R\left(\mathbf{m},\widehat{\mathbf{h}}\right) = \sum_{\widehat{\mathbf{m}}} \widehat{U}\left[\widehat{\mathbf{m}},\widehat{\mathbf{h}}, t_s\left(\mathbf{m},\widehat{\mathbf{m}}-\widehat{\mathbf{h}}\right) + t_r\left(\mathbf{m},\widehat{\mathbf{m}}+\widehat{\mathbf{h}}\right)\right] , \qquad (36)$$

where $\widehat{U}\left(\widehat{\mathbf{m}},\widehat{\mathbf{h}},t\right)$ is the recorded wavefield at the surface as a function of surface midpoint $\widehat{\mathbf{m}}$ and offset $\widehat{\mathbf{h}}$ (Figure 6). t_s and t_r stand for traveltimes from sources and receivers at coordinates $\widehat{\mathbf{m}}-\widehat{\mathbf{h}}$ and $\widehat{\mathbf{m}}+\widehat{\mathbf{h}}$ to points in the subsurface at coordinates $\mathbf{m}$. For simplicity, the amplitude and phase correction term $A\left(\mathbf{m},\widehat{\mathbf{m}},\widehat{\mathbf{h}}\right)\frac{\partial}{\partial t}$ is omitted in equation (36). The time-shift imaging condition can be implemented in Kirchhoff
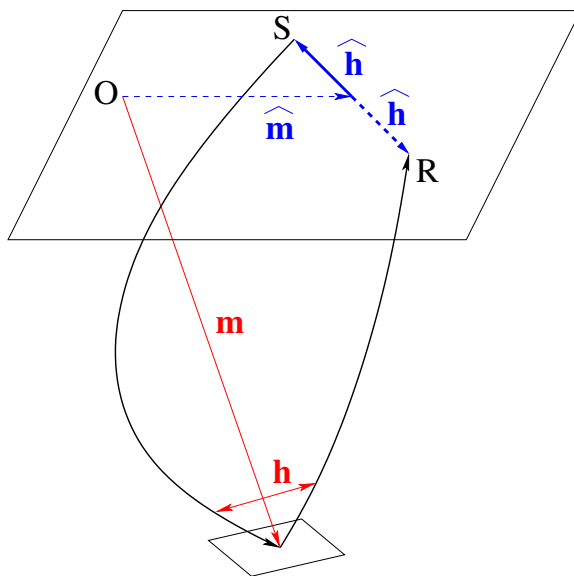

Figure 6: Notations for Kirchhoff imaging. S is a source and R is a receiver.

imaging using a modification of equation (36) that is equivalent to equations (6) and (8):

$$R\left(\mathbf{m},\tau\right) = \sum_{\widehat{\mathbf{m}}} \sum_{\widehat{\mathbf{h}}} \widehat{U}\left[\widehat{\mathbf{m}},\widehat{\mathbf{h}}, t_s\left(\mathbf{m},\widehat{\mathbf{m}}-\widehat{\mathbf{h}}\right) + t_r\left(\mathbf{m},\widehat{\mathbf{m}}+\widehat{\mathbf{h}}\right) + 2\tau\right] . \qquad (37)$$

Images obtained by Kirchhoff migration as discussed in equation (37) differ from image constructed with equation (36). Relation (37) involves a double summation over surface midpoint $\widehat{\mathbf{m}}$ and offset $\widehat{\mathbf{h}}$ to produce an image at location $\mathbf{m}$. Therefore, the entire input data contributes potentially to every image location. This is advantageous because migrating using relation (36) different offsets $\widehat{\mathbf{h}}$ independently may lead to imaging artifacts as discussed by Stolk and Symes (2004). After Kirchhoff migration using relation (37), images can be converted to the angle domain using equation (23).

EXAMPLES

We demonstrate the imaging condition introduced in this paper with the Sigsbee 2A synthetic model (Paffenholz et al., 2002). Figure 7 shows the correct migration velocity and the image created by shot-record migration with wavefield extrapolation using the time-shift imaging condition introduced in this paper. The image in the bottom panel of Figure 7 is extracted at $\tau = 0$.

The top row of Figure 8 shows common-image gathers at locations $x = \{7, 9, 11, 13, 15, 17\}$ km obtained by time-shift imaging condition. As in the preceding synthetic example, we can observe events with linear trends at slopes corresponding to local migration velocity. Since the migration velocity is correct, the strongest events in common-image gathers correspond to $\tau = 0$. For comparison, the bottom row of Figure 8 shows common-image gathers at the same locations obtained by space-shift imaging condition. In the later case, the strongest events occur at $\mathbf{h} = 0$. The zero-offset images ($\tau = 0$ and $\mathbf{h} = 0$) are identical.

Figure 9 shows the angle-decomposition for the common-image gather at location $x = 7$ km. From left to right, the panels depict the migrated image, a common-image gather resulting from migration by wavefield extrapolation with time-shift imaging, the common-image gather after slant-stacking in the $z - \tau$ plane, and an angle-gather derived from the slant-stacked panel using equation equation (23).

For comparison, Figure 10 depicts a similar process for a common-image gather at the same location obtained by space-shift imaging. Despite the fact that the offset gathers are completely different, the angle-gathers are comparable showing similar trends of angle-dependent reflectivity.

The top row of Figure 11 shows angle-domain common-image gathers for time-shift imaging at locations $x = \{7, 9, 11, 13, 15, 17\}$ km. Since the migration velocity is correct, all events are mostly flat indicating correct imaging. For comparison, the bottom row of Figure 11 shows angle-domain common-image gathers for space-shift imaging condition at the same locations in the image.

Finally, we illustrate the behavior of time-shift imaging with incorrect velocity. The top panel in Figure 12 shows an incorrect velocity model used to image the Sigsbee 2A data, and the bottom panel shows the resulting image. The incorrect velocity is a smooth version of the correct interval velocity, scaled by 10% from a depth $z = 5$ km downward. The uncollapsed diffractors at depth $z = 7$ km clearly indicate velocity inaccuracy.

Figures 13 and 14 show imaging gathers and the derived angle-gathers for time-shift and space-shift imaging at the same location $x = 7$ km. Due to incorrect velocity, focusing does not occur at $\tau = 0$ or $\mathbf{h} = 0$ as in the preceding case. Likewise, the reflections in angle-gathers are non-flat, indicating velocity inaccuracies. Compare Figures 9 and 13, and Figures 10 and 14. Those moveouts can be exploited for migration velocity analysis (Biondi and Sava, 1999; Sava and Biondi, 2004a,b; Clapp et al., 2004).
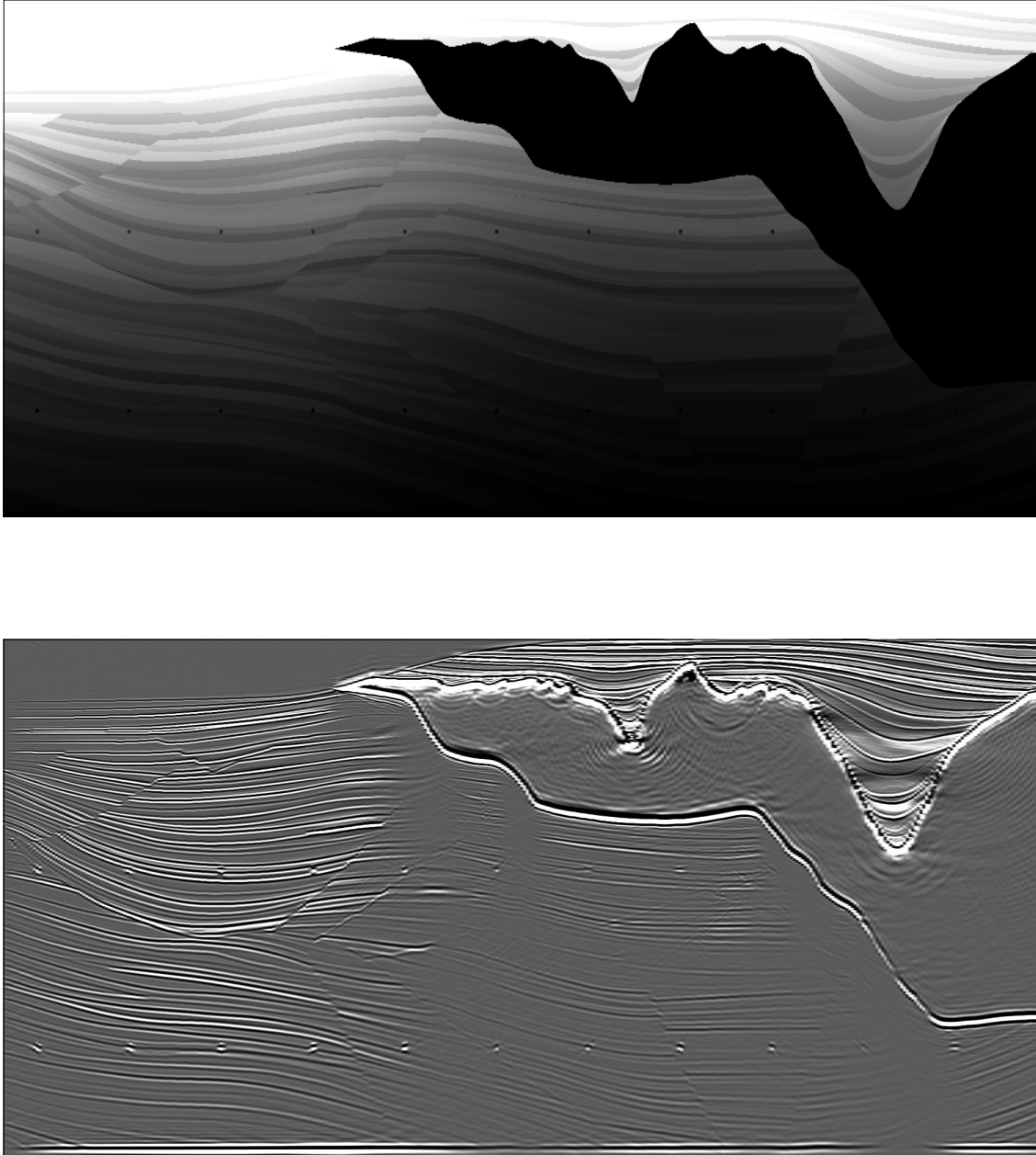
Figure 7: Sigsbee 2A model: correct velocity (top) and migrated image obtained by shot-record wavefield extrapolation migration with time-shift imaging condition (bottom).
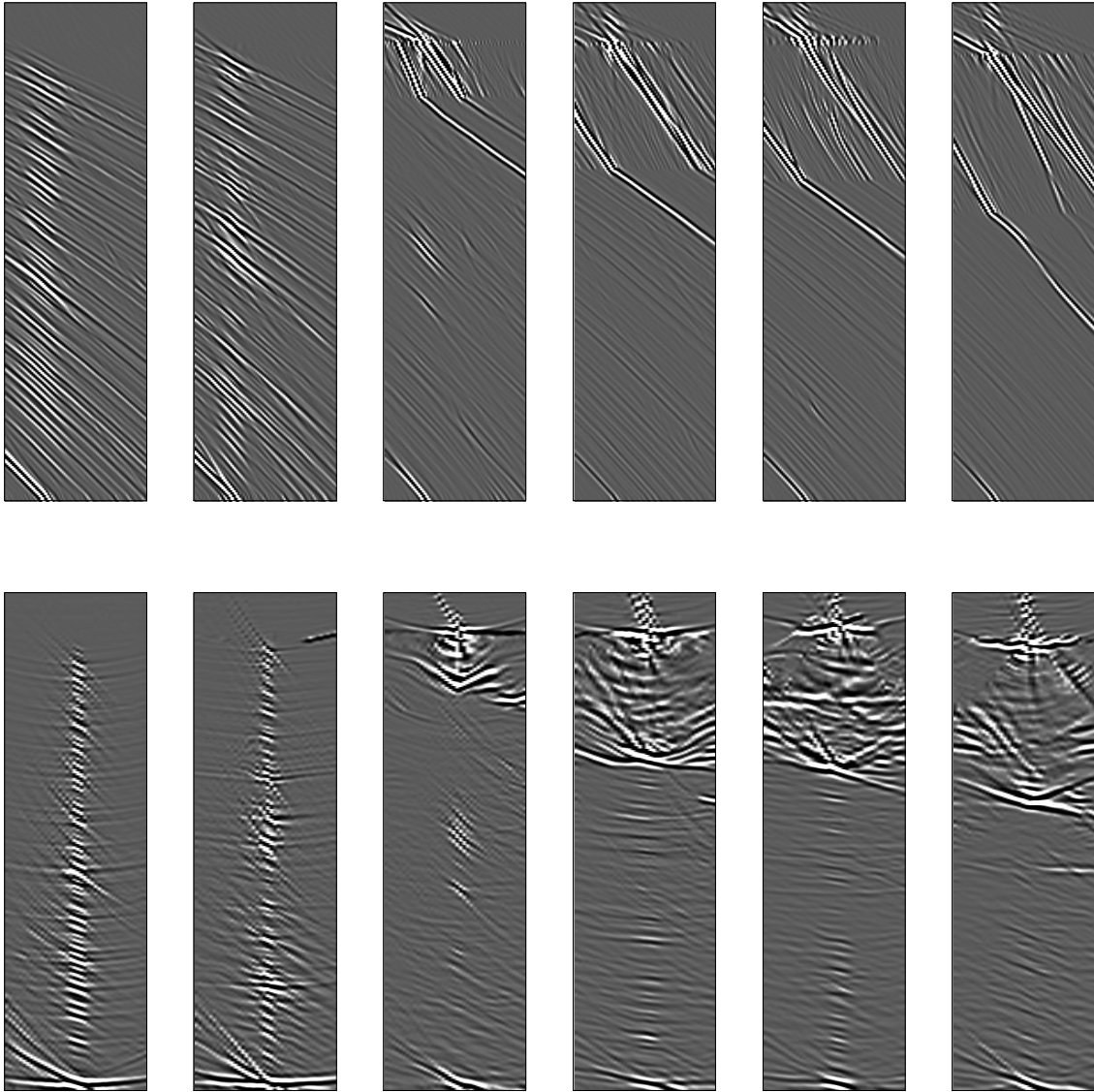
Figure 8: Imaging gathers at positions $x = \{7, 9, 11, 13, 15, 17\}$ km. Time-shift imaging condition (top row), and space-shift imaging condition (bottom row).
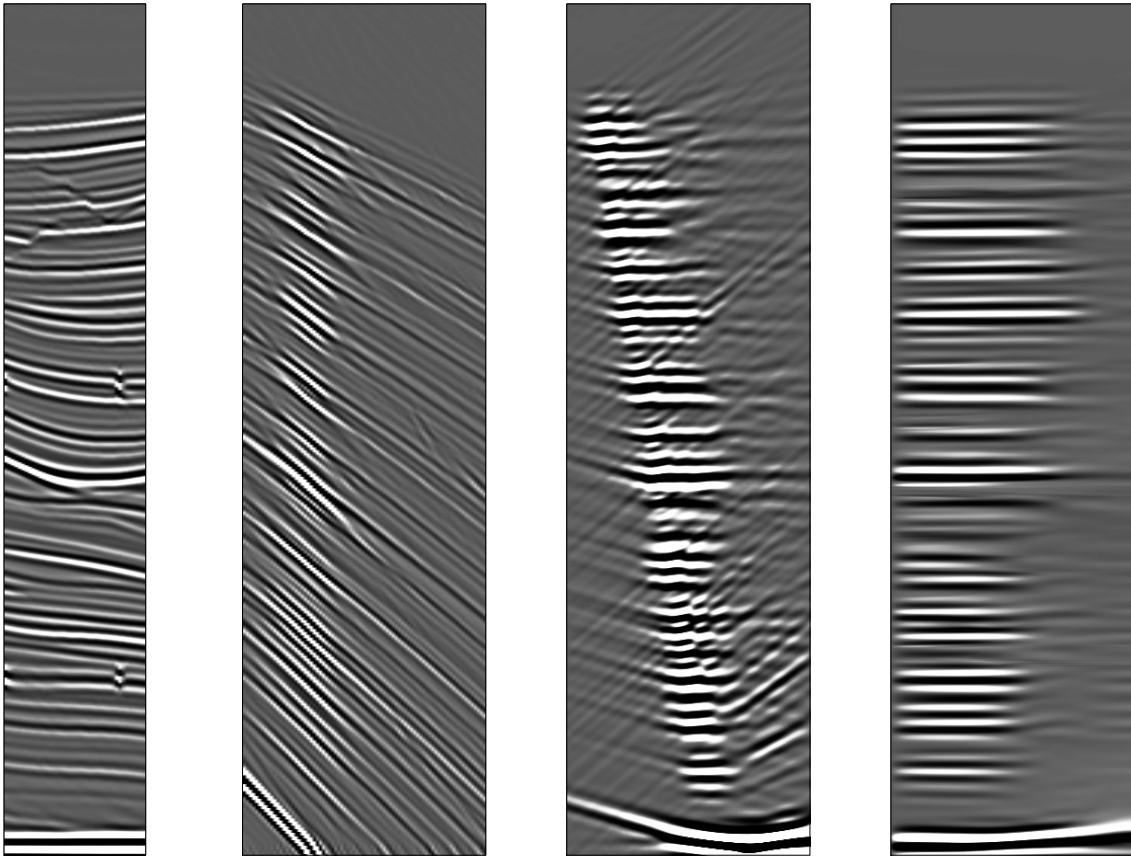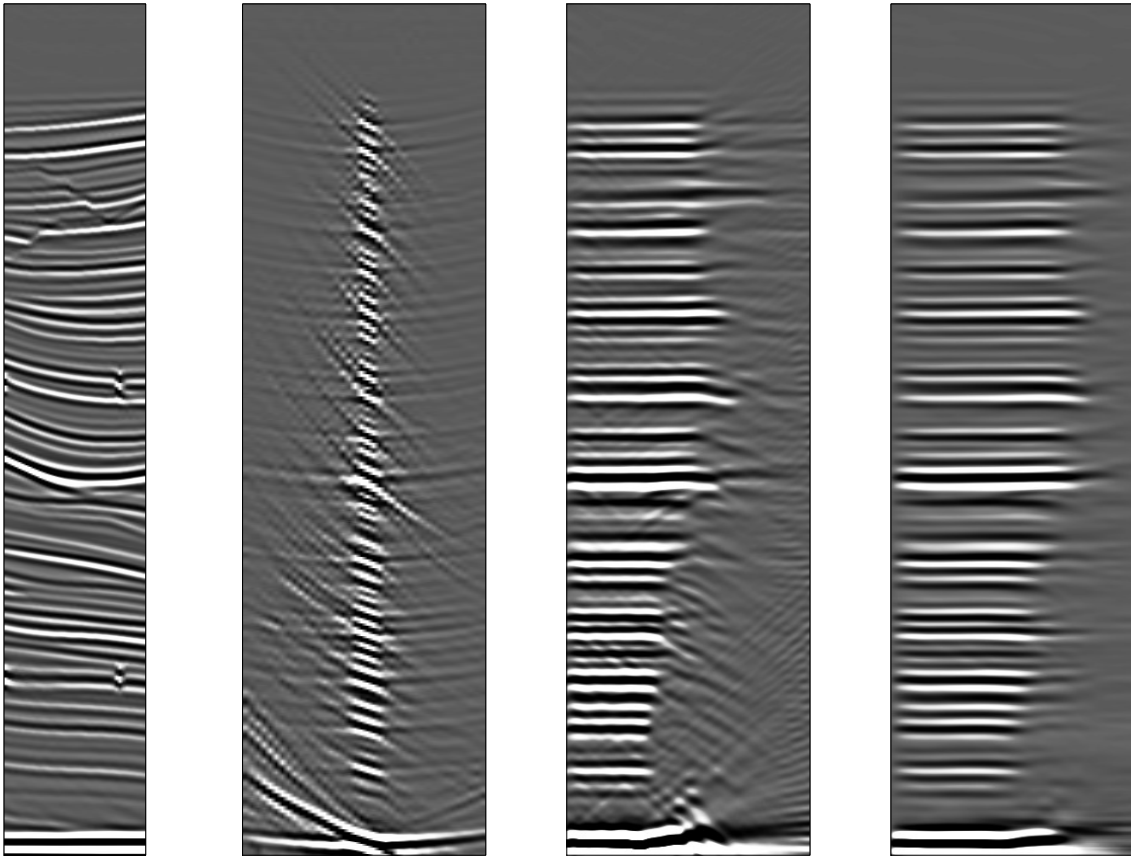
Figure 9: Time-shift imaging condition gather at $x = 7$ km. From left to right, the panels depict the image, the time-shift gather, the slant-stacked time-shift gather and the angle-gather.

Figure 10: Space-shift imaging condition gather at $x = 7$ km: From left to right, the panels depict the image, the space-shift gather, the slant-stacked space-shift gather and the angle-gather.
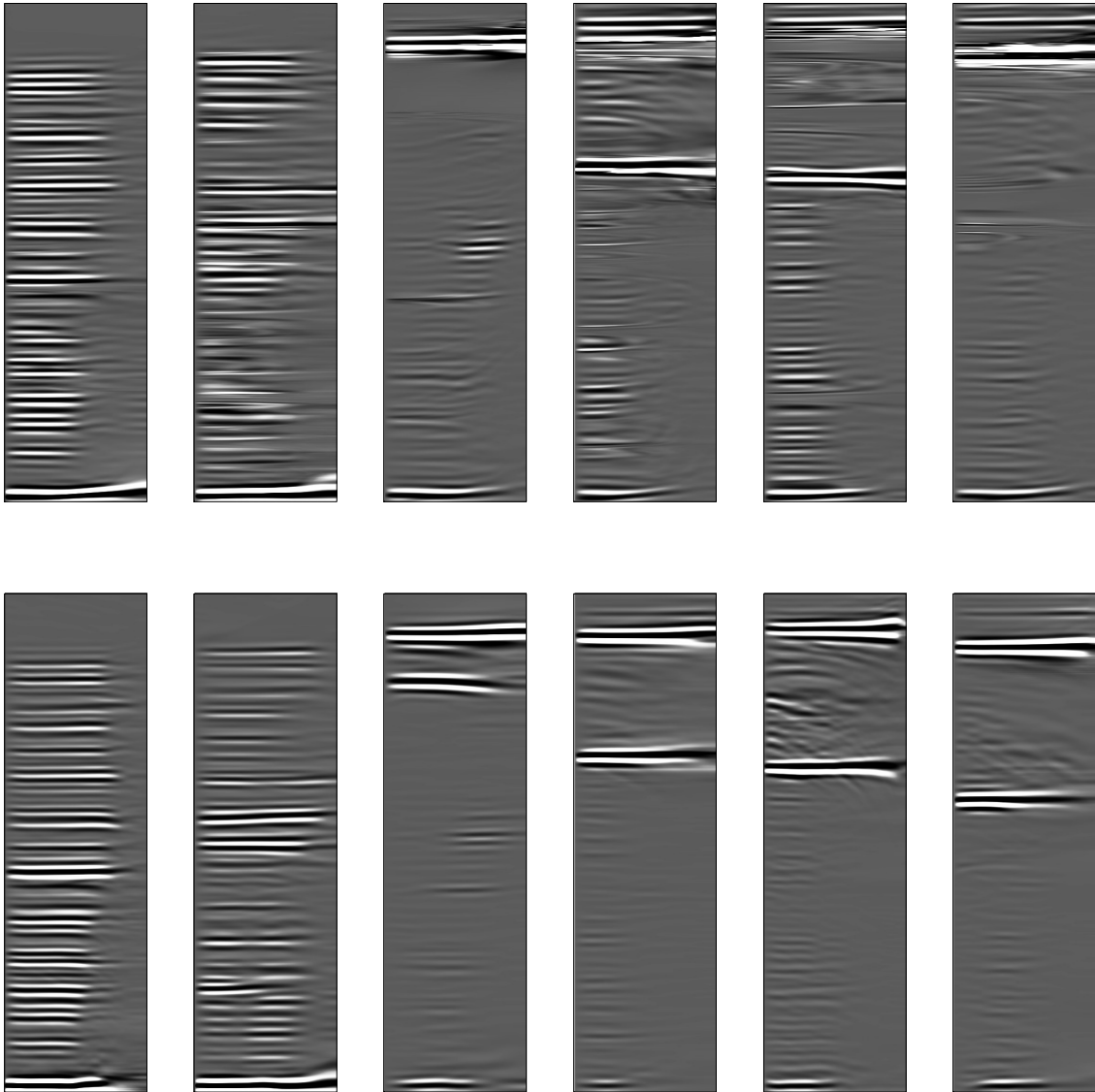
Figure 11: Angle-gathers at positions $x = \{7, 9, 11, 13, 15, 17\}$ km. Time-shift imaging condition (top row), and space-shift imaging condition (bottom row). Compare with Figure 8.
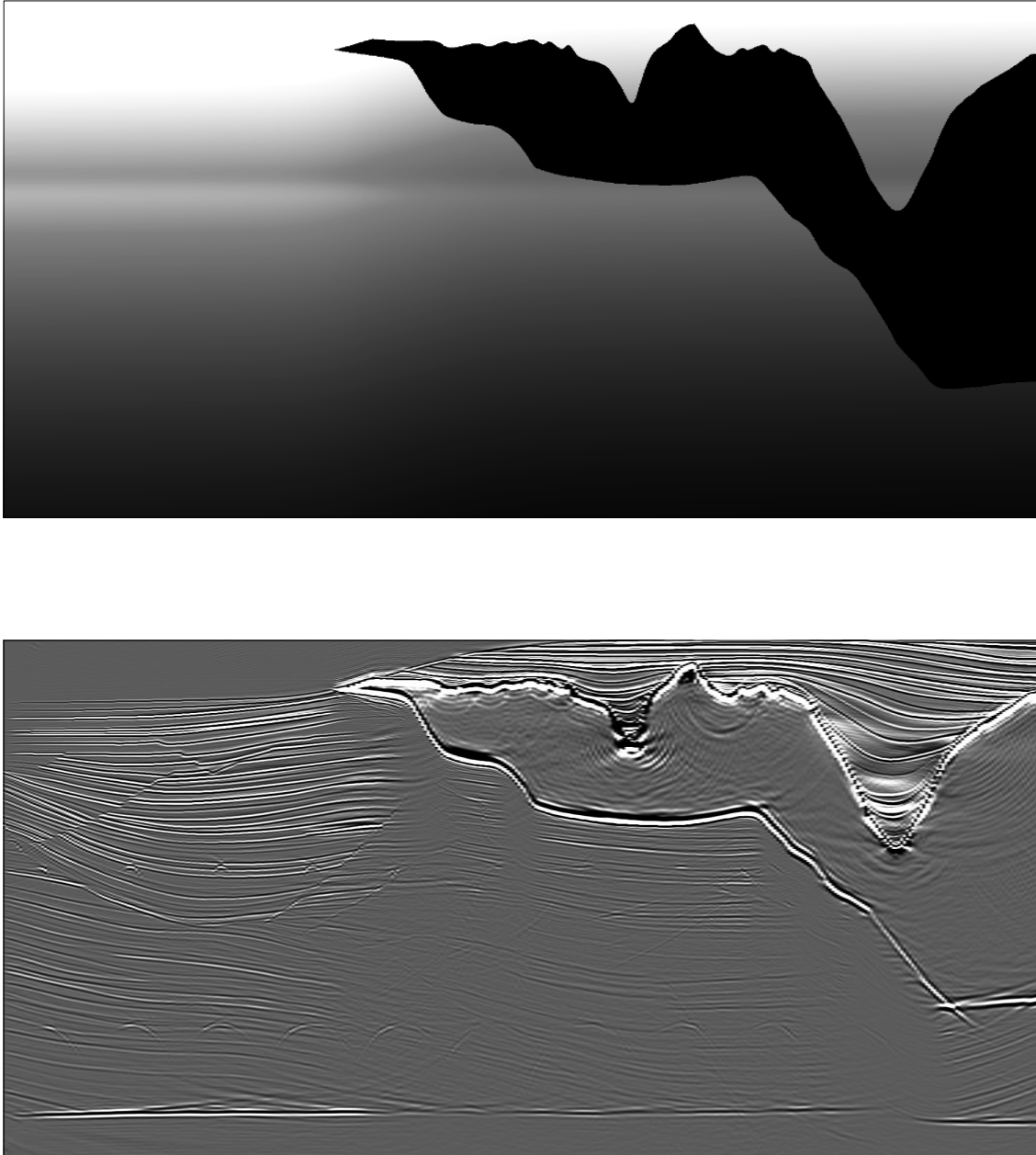
Figure 12: Sigsbee 2A model: incorrect velocity (top) and migrated image obtained by shot-record wavefield extrapolation migration with time-shift imaging condition. Compare with Figure 7.
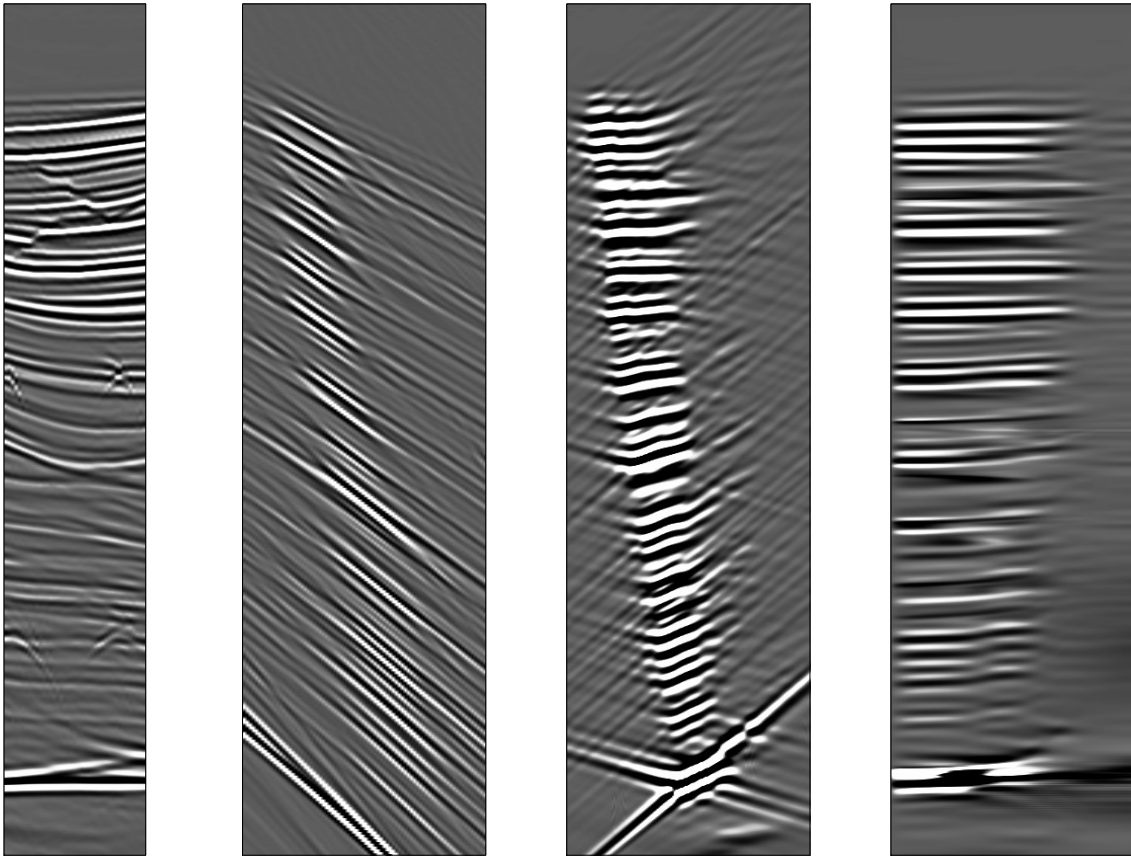
Figure 13: Time-shift imaging condition gather at $x = 7$ km. From left to right, the panels depict the image, the offset-gather, the slant-stacked gather and the angle-gather. Compare with Figure 9.
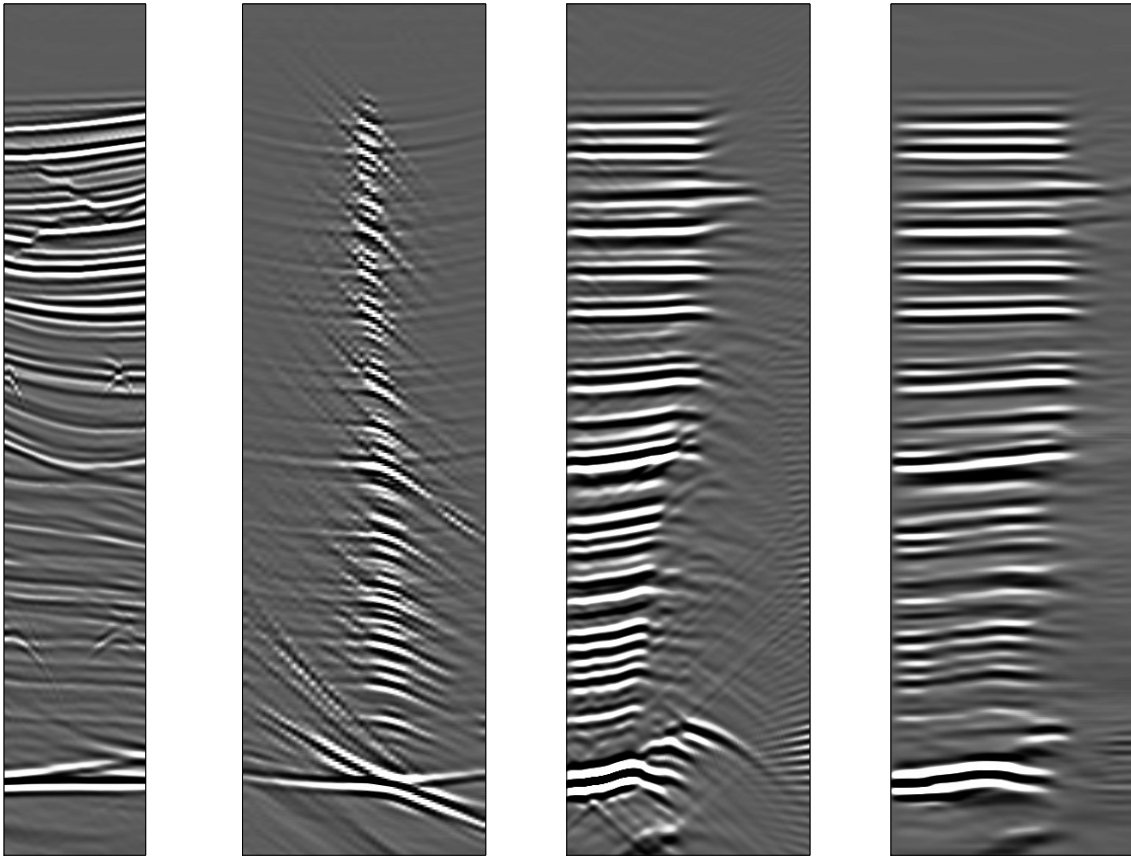
Figure 14: Space-shift imaging condition gather at $x = 7$ km. From left to right, the panels depict the image, the offset-gather, the slant-stacked gather and the angle-gather. Compare with Figure 10.

DISCUSSION

As discussed in one of the preceding sections, time-shift gathers consist of linear events with slopes corresponding to the local migration velocity. In contrast, space-shift gathers consist of events focused at $\mathbf{h} = 0$. Those events can be mapped to the angle-domain using transformations (20) and (23), respectively.

In order to understand the angle-domain mapping, we consider a simple synthetic in which we model common-image gathers corresponding to incidence at a particular angle. The experiment is depicted in Figure 15 for time-shift imaging, and in Figure 16 for space-shift imaging. For this experiment, the sampling parameters are the following: $\Delta z = 0.01$ km, $\Delta h = 0.02$ km, and $\Delta \tau = 0.01$ s.

A reflection event at a single angle of incidence maps in common-image gathers as a line of a given slope. The left panels in Figures 15 and 16 show 3 cases, corresponding to angles of $0°$, $20°$ and $40°$. Since we want to analyze how such events map to angle, we subsample each line to 5 selected samples lining-up at the correct slope.

The middle panels in Figures 15 and 16 show the data in the left panels after slant-stacking in $z - \tau$ or $z - h$ panels, respectively. Each individual sample from the common-image gathers maps in a line of a different slope intersecting in a point. For example, normal incidence in a time-shift gather maps at the migration velocity $\nu = 2$ km/s (Figure 15 top row, middle panel), and normal incidence in a space-shift gather maps at slant-stack parameter $\tan \theta = 0$.

The right panels in Figures 15 and 16 show the data from the middle panels after mapping to angle using equations (23) and (20), respectively. All lines from the slant-stack panels map into curves that intersect at the angle of incidence.

We note that all curves for the time-shift angle-gathers have zero curvature at normal incidence. Therefore, the resolution of the time-shift mapping around normal incidence is lower than the corresponding space-shift resolution. However, the storage and computational cost of time-shift imaging is smaller than the cost of equivalent space-shift imaging. The choice of the appropriate imaging condition depends on the imaging objective and on the trade-off between the cost and the desired resolution.

CONCLUSIONS

We develop a new imaging condition based on time-shifts between source and receiver wavefields. This method is applicable to Kirchhoff, reverse-time and wave-equation migrations and produces common-image gathers indicative of velocity errors. In wave-equation migration, time-shift imaging is more efficient than space-shift imaging, since it only involves a simple phase shift prior to the application of the usual imaging cross-correlation. Disk storage is also reduced, since the output volume depends on only one parameter (time-shift τ) instead of three parameters (space-shift $\mathbf{h}$). We show how this imaging condition can be used to construct angle-gathers from time-shift
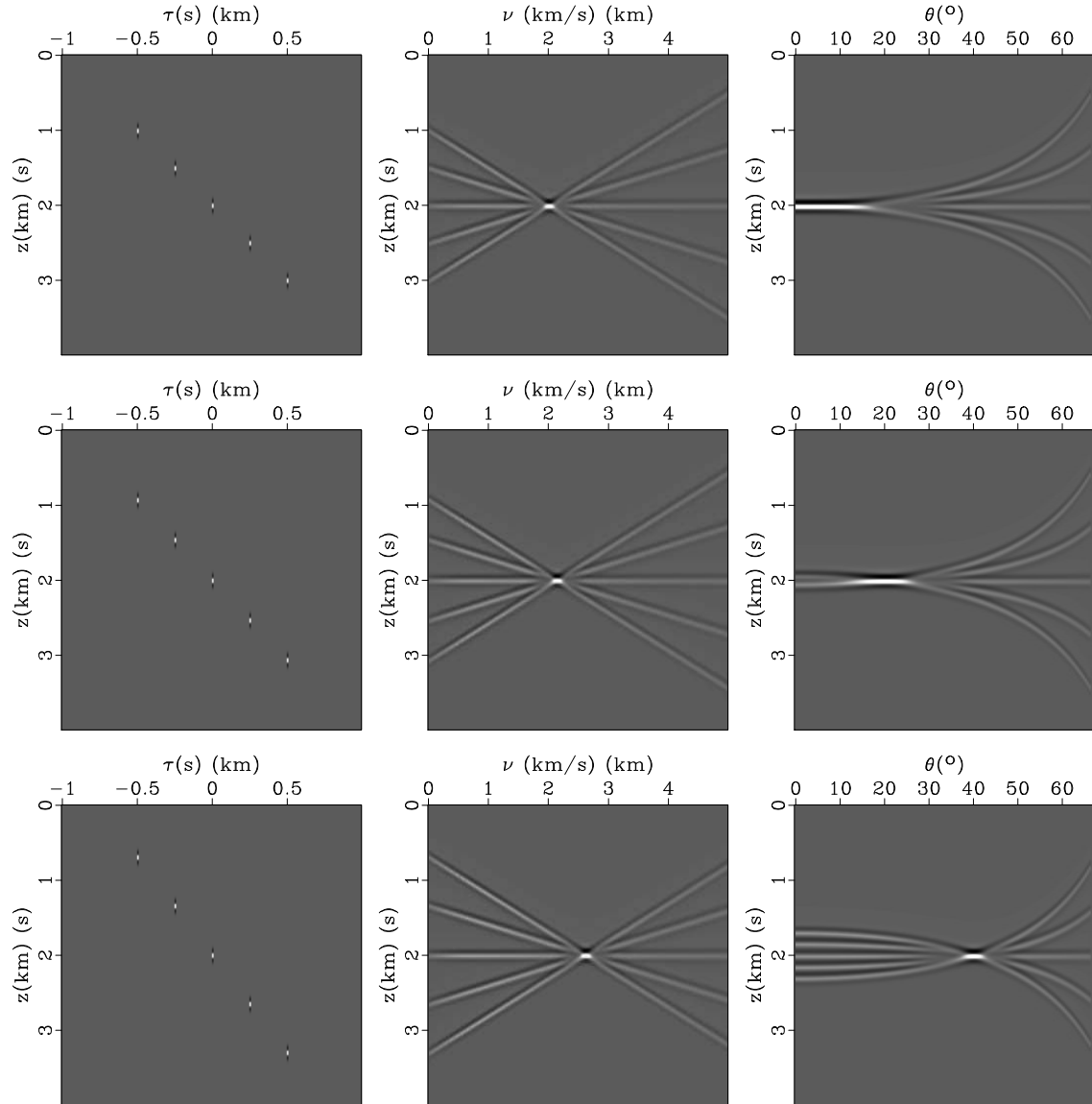
Figure 15: Image-gather formation using time-shift imaging. Each row depicts an event at 0° (top), 20° (middle), and 40° (bottom). Three columns correspond to sub-sampled time-shift gathers (left), slant-stacked gathers (middle), and angle-gathers (right).

Figure 16: Image-gather formation using space-shift imaging. Each row depicts an event at 0° (top), 20° (middle), and 40° (bottom). Three columns correspond to subsampled space-shift gathers (left), slant-stacked gathers (middle), and angle-gathers (right).
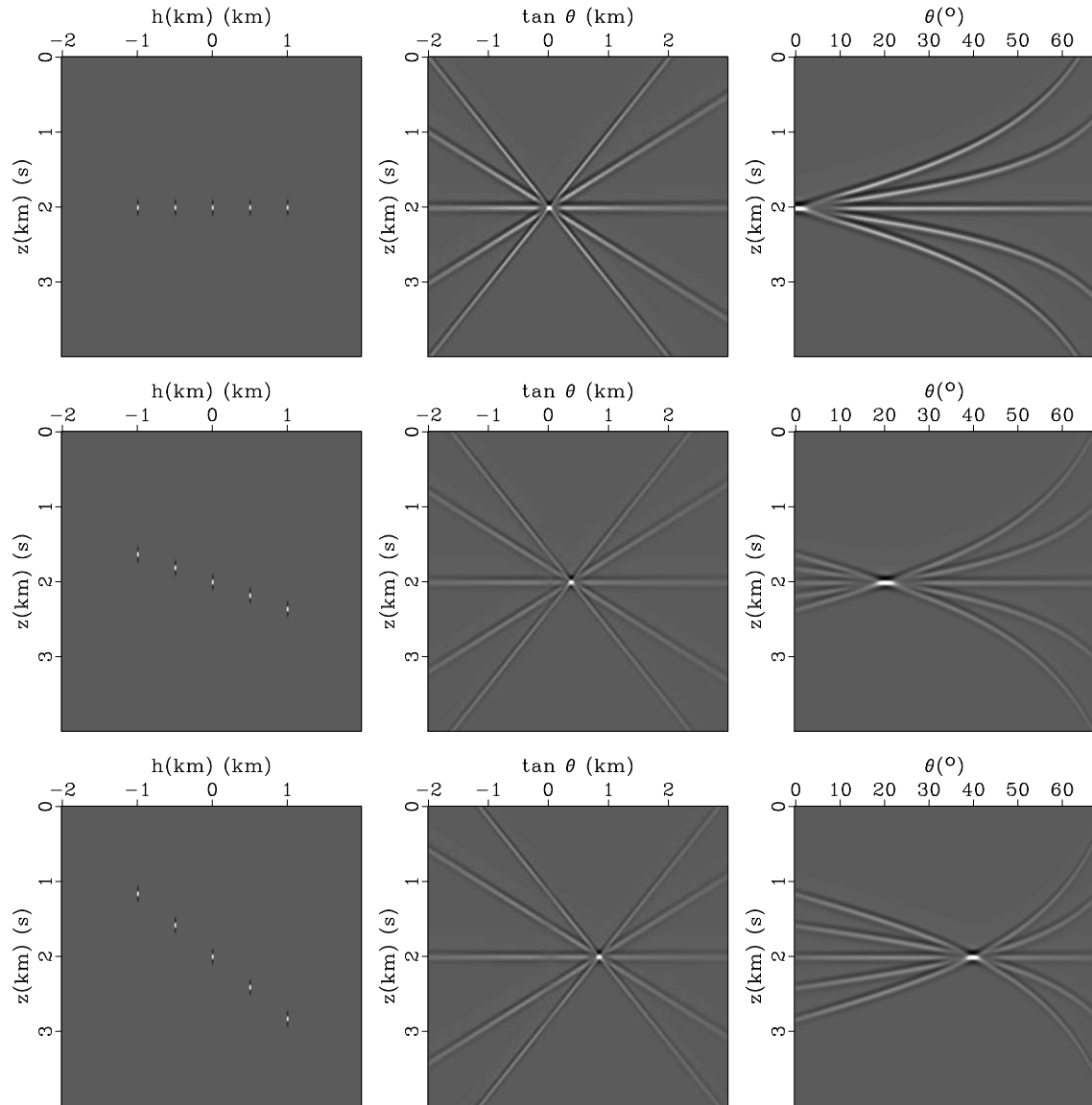
gathers. More research is needed on how to utilize this new imaging condition for velocity and amplitude analysis.

ACKNOWLEDGMENT

REFERENCES

Bartana, A., D. Kosloff, and I. Ravve, 2005, On angle-domain common-image gathers by wavefield continuation methods: Geophysics, submitted.

Biondi, B., and P. Sava, 1999, Wave-equation migration velocity analysis: 69th Ann. Internat. Mtg, Soc. of Expl. Geophys., 1723–1726.

Biondi, B., and W. Symes, 2004, Angle-domain common-image gathers for migration velocity analysis by wavefield-continuation imaging: Geophysics, **69**, 1283–1298.

Claerbout, J. F., 1985, Imaging the Earth's Interior: Blackwell Scientific Publications.

Clapp, R. G., B. Biondi, and J. F. Claerbout, 2004, Incorporating geologic information into reflection tomography: Geophysics, **69**, 533–546.

de Bruin, C. G. M., C. P. A. Wapenaar, and A. J. Berkhout, 1990, Angle-dependent reflectivity by means of prestack migration: Geophysics, **55**, 1223–1234.

Faye, J. P., and J. P. Jeannot, 1986, Prestack migration velocities from focusing depth analysis: 56th Ann. Internat. Mtg., Soc. of Expl. Geophys., Session:S7.6.

Fomel, S., 2004, Theory of 3-D angle gathers in wave-equation imaging, *in* 74th Ann. Internat. Mtg.: Soc. of Expl. Geophys.

MacKay, S., and R. Abma, 1992, Imaging and velocity estimation with depth-focusing analysis: Geophysics, **57**, 1608–1622.

——, 1993, Depth-focusing analysis using a wavefront-curvature criterion: Geophysics, **58**, 1148–1156.

Mosher, C., and D. Foster, 2000, Common angle imaging conditions for prestack depth migration: 70th Ann. Internat. Mtg, Soc. of Expl. Geophys., 830–833.

Nemeth, T., 1995, Velocity estimation using tomographic depth-focusing analysis: 65th Ann. Internat. Mtg, Soc. of Expl. Geophys., 465–468.

——, 1996, Relating depth-focusing analysis to migration velocity analysis: 66th Ann. Internat. Mtg, Soc. of Expl. Geophys., 463–466.

Paffenholz, J., B. McLain, J. Zaske, and P. Keliher, 2002, Subsalt multiple attenuation and imaging: Observations from the Sigsbee2B synthetic dataset: 72nd Annual International Meeting, SEG, Soc. of Expl. Geophys., 2122–2125.

Prucha, M., B. Biondi, and W. Symes, 1999, Angle-domain common image gathers by wave-equation migration: 69th Ann. Internat. Mtg, Soc. of Expl. Geophys., 824–827.

Rickett, J. E., and P. C. Sava, 2002, Offset and angle-domain common image-point gathers for shot-profile migration: Geophysics, **67**, 883–889.

Sava, P., and B. Biondi, 2004a, Wave-equation migration velocity analysis - I: Theory: Geophysical Prospecting, **52**, 593–606.

———, 2004b, Wave-equation migration velocity analysis - II: Subsalt imaging examples: Geophysical Prospecting, **52**, 607–623.

Sava, P., and S. Fomel, 2005, Coordinate-independent angle-gathers for wave equation migration, *in* 75th Ann. Internat. Mtg.: Soc. of Expl. Geophys.

Sava, P. C., and S. Fomel, 2003, Angle-domain common-image gathers by wavefield continuation methods: Geophysics, **68**, 1065–1074.

Soubaras, R., 2003, Angle gathers for shot-record migration by local harmonic decomposition: 73rd Ann. Internat. Mtg., Soc. of Expl. Geophys., 889–892.

Stolk, C. C., and W. W. Symes, 2004, Kinematic artifacts in prestack depth migration: Geophysics, **69**, 562–575.

Xie, X., and R. Wu, 2002, Extracting angle domain information from migrated wavefield, *in* 72nd Ann. Internat. Mtg.: Soc. of Expl. Geophys., 1360–1363.